Eur. Phys. J. B **26**, 515–520 (2002)
DOI: 10.1140/epjb/e20020121

THE EUROPEAN PHYSICAL JOURNAL B
EDP Sciences

Electric Nusselt number characterization of electroconvection in nematic liquid crystals

J.T. Gleeson[1], N. Gheorghiu[1], and E. Plaut[2,a]

[1] Department of Physics, Kent State University, Kent, OH 44242 USA
[2] LEMTA, INPL - UHP - CNRS, 2 avenue de la Forêt de Haye, 54504 Vandœuvre Cedex, France

Received 21 January 2001 and Received in final form 1st February 2002

Abstract. We develop a characterization method of electroconvection structures in a planar nematic liquid crystal layer by a study of the electric current transport. Because the applied potential difference has a sinusoidal time dependence, we define two electric Nusselt numbers corresponding to the in-phase and out-of-phase components of the current. These Nusselt numbers are predicted theoretically using a weakly nonlinear analysis of the standard model. Our measurements of the electric current confirm that both numbers vary linearly with the distance from onset until the occurence of secondary transitions. A systematic comparison between our theoretical and experimental results, using no adjusted parameters, demonstrates moderate agreement, but discrepancies remain. Electric transport measurements during electroconvection represent a quantitative test of the standard model completely independent from optical probes. Thus, the technique described here can be a useful complement to traditional structural measurements.

PACS. 47.54.+r Pattern selection; pattern formation – 61.30.-v Liquid crystals – 47.20.Ky Nonlinearity (including bifurcation theory)

1 Introduction

Pattern formation within structureless environments pervades nature, and in order to develop a better understanding of these phenomena well-controlled experimental systems exhibiting pattern formation are extensively studied. Among these, thermoconvection of a layer of fluid heated from below [1] and electroconvection of a nematic liquid crystal layer [2,3] are particularly interesting since they allow very large aspect ratio geometries. In both systems, convection structures form spontaneously when the applied stress, *i.e.* the gradient of either the temperature or the electric potential, exceeds a critical value. These inherently non-equilibrium structures can only persist when there is an energy source to overcome the dissipation associated with the flow. Therefore, energy transport studies represent a particularly valuable technique for elucidating the mechanisms that lead to these patterns. For example, the first accurate determination of the stress necessary to induce thermoconvection was made by measuring the heating power required to sustain a desired temperature difference across a thin layer of water [4]. This power is customarily expressed as the Nusselt number, defined as the heat flow across a fluid layer relative to the heat flow required in the absence of fluid flow. Nusselt number measurements remain a method of choice for studies not only of the structured states that occur during thermoconvection when the stress is only slightly above its critical value [5] but also of the turbulent flow that occurs when the stress is enormous [6]. By contrast, until recently the electroconvection of a planar nematic liquid crystal layer, which represents a similar but fully *anisotropic* model pattern forming system, has been studied only with qualitative or semi-quantitative optical techniques, which become fully quantitative in the vicinity of the threshold only [7]. We propose in this work, following the pioneering studies [8–10] and the more recent experiments [11,12], to use instead global electric flow measurements as a characterization method. In addition to the connection with energy dissipation (see (5)), the interest of such measurements is that they can be very precise, regardless of how complicated the spatio-temporal convective structures may be. Thus energy transport measurements open the way to a better characterization of the various chaotic or turbulent regimes that occur in electroconvection and are still not completely understood, see *e.g.* [13,14]. One deficiency of the existing studies of global electric flow is the absence of comparison between experiments and theory. The aim of this work is to fill this gap by focusing on the weakly nonlinear regime close to the onset of convection, where stationary convective structures develop, and consequently a quantitative comparison becomes possible.

Electroconvection is obtained when an a.c. electric potential, $\sqrt{2}V\cos(\omega t)$, is applied to two horizontal ($\perp \hat{\mathbf{z}}$) electrodes separated by distance d confining a nematic

[a] e-mail: emmanuel.plaut@ensem.inpl-nancy.fr

liquid crystal. Here we focus on the *planar* anchoring case where the director field $\mathbf{n}$ is fixed to $\hat{\mathbf{x}}$ at the confining electrode plates. The instability relies on a coupling between $\mathbf{n}$, the velocity field $\mathbf{v}$ and the induced charge density ρ_e or equivalently the induced electric potential ϕ, such that the full electric field reads $\mathbf{E} = \sqrt{2}V/d\,[\cos(\omega t)\hat{\mathbf{z}} - d\boldsymbol{\nabla}\phi]$. At moderate frequencies ω, of the order of the inverse of the *charge-diffusion time* $\tau_0 = \epsilon_\perp/\sigma_\perp$ with $\epsilon_\perp$ ($\sigma_\perp$) the dielectric permittivity (conductivity) perpendicular to $\mathbf{n}$, when V exceeds a critical value V_c , the instability sets in the form of normal *conduction* rolls of wavevector $\mathbf{q} = q\hat{\mathbf{x}}$; at large frequencies *dielectric* rolls are observed [3] but we do not consider this regime in this work. These phenomena are well explained *via* the standard model (SM) for electroconvection [3,10,15]. In addition to linear properties (values of V_c and q as a function of ω), the SM explains several secondary instabilities that are experimentally observed, such as the transitions to zig-zag rolls, stationary and oscillatory bimodal patterns and abnormal rolls [16]. In Section 2 we will therefore present a SM theoretical analysis of the current flowing in an electroconvection cell, and propose natural definitions for the electric Nusselt numbers. Our experimental methods will be described in Section 3. The experimental and theoretical results will be compared in Section 4.

2 Theoretical calculations

2.1 General considerations and definitions

The total current I through the nematic cell enclosed by the horizontal electrodes of area S can be calculated as the circulation of the magnetic field $\mathbf{H}$. From the Maxwell-Ampère equation, $\boldsymbol{\nabla} \times \mathbf{H} = \mathbf{j} + \partial_t \mathbf{D}$, I is sum of the conduction and displacement currents:

$$I \;=\; \iint_S \left(j_z \;+ \partial_t D_z\right) \mathrm{d}x\; \mathrm{d}y \qquad (1)$$

where, within the SM, $\mathbf{j} \;=\; \sigma_\perp \mathbf{E} + \sigma_a(\mathbf{n}\cdot\mathbf{E})\mathbf{n} + \rho_e \mathbf{v}$; $\mathbf{D} \;=\; \epsilon_\perp \mathbf{E} + \epsilon_a(\mathbf{n}\cdot\mathbf{E})\mathbf{n}$; $\sigma_a = \sigma_\parallel - \sigma_\perp$ and $\epsilon_a = \epsilon_\parallel - \epsilon_\perp$ with $\sigma_\parallel$ ($\epsilon_\parallel$) the conductivity (dielectric permittivity) parallel to $\mathbf{n}$. Note that the surface integral in (1) does not depend on the z-value ($-d/2 \le z \le d/2$) chosen, because of the Maxwell-Ampère equation. In the quiescent (no convection) state $\mathbf{n} = \hat{\mathbf{x}}$, $\mathbf{v} = \mathbf{0}$ and $\phi = 0$, therefore

$$I = I^0 = I_r^0 \cos(\omega t) - I_i^0 \sin(\omega t) = \frac{\sqrt{2}VS}{d}\,[\sigma_\perp \cos(\omega t) - \epsilon_\perp \omega \sin(\omega t)]. \qquad (2)$$

In the convecting state all fields $\mathbf{n}, \mathbf{v}$ and ϕ are modified, as is I. Within the SM, for homogeneous stationary roll solutions

$$I = I_r \cos(\omega t) - I_i \sin(\omega t) + \textit{higher temporal harmonics} \qquad (3)$$

where the amplitudes of the higher temporal harmonics are expected to be much smaller than I_r and I_i, at least at moderate frequencies [17]. We define the real and imaginary reduced Nusselt numbers as

$$\mathcal{N}_r \;=\; \frac{I_r}{I_r^0} - 1 \;\text{ and }\; \mathcal{N}_i \;=\; \frac{I_i}{I_i^0} - 1, \qquad (4)$$

respectively. Thus $\mathcal{N}_r = \mathcal{N}_i = 0$ in the quiescent state, while in the convecting state $\mathcal{N}_r$ measures the excess energy dissipation due to convection of the nematic liquid crystal, that is the time average

$$\left\langle \sqrt{2}V \cos(\omega t) I(t) \right\rangle_t \;=\; (1+\mathcal{N}_r) V^2 \sigma_\perp S/d. \qquad (5)$$

In heuristic terms the effective conductivity of the nematic layer is changed by convection from $\sigma_\perp$ to $\sigma_\perp(1+\mathcal{N}_r)$; equivalently the imaginary Nusselt number measures the change in the effective permittivity of the nematic layer, $\epsilon_\perp$ in the quiescent state, $\epsilon_\perp(1+\mathcal{N}_i)$ in the convecting state.

2.2 Weakly nonlinear regime

When the reduced distance from onset $\epsilon \;\equiv\; V^2/V_c^2 - 1$ is small, the electric Nusselt numbers can be calculated for roll structures using *weakly nonlinear methods*. Assuming that the leading convection amplitude, A, associated with the critical roll mode, remains small, a systematic expansion in powers of A is performed. After adiabatic elimination of the slave modes and calculation of the corresponding amplitude equation, an approximate roll solution is obtained together with the relation $A(\epsilon) = a\sqrt{\epsilon}$. The current can then be calculated from (1). For symmetry reasons the first contribution from the convection modes comes at order A^2, and therefore one expects $\mathcal{N}_r = n_r A^2 = n_r a^2 \epsilon$, $\mathcal{N}_i = n_i A^2 = n_i a^2 \epsilon$ in the weakly nonlinear regime. That is, Nusselt numbers allow a direct measurement of the convection amplitude A, and therefore a test of the supercritical law $A(\epsilon) = a\sqrt{\epsilon}$. On the other hand, the signs and the relative magnitude of $\mathcal{N}_r$ and $\mathcal{N}_i$ are only controlled by the form of the critical roll mode, no matter the value of a.

In order to obtain *approximate, unscaled analytic formulae* demonstrating the various contributions to the Nusselt numbers, we can use the quasi-unidimensional approximation. The analytic results thus obtained are useful for illustrative purposes; the sophisticated numerical techniques used to calculate Nusselt numbers to compare with experiments will be described subsequently. In the quasi-unidimensional approximation, all fields are considered at the middle of the layer ($z = 0$) and only their x-dependence is kept. The critical normal roll mode then assumes the form

$$n_z = -AN_z \sin(qx), \quad v_z = \frac{A}{q\tau_0} V_z \cos(qx), \quad \phi = \frac{A}{qd}[\Phi_c \cos(\omega t) + \Phi_s \sin(\omega t)] \cos(qx), \qquad (6)$$

where $q \simeq \pi/d$ and, as in the rest of our theoretical calculations, we only keep the lowest nontrivial time-mode

for each field. We also choose as a normalization condition $N_z = 1$; then V_z , Φ_c and Φ_s are calculated at fixed frequency by solving the neutral stability eigenvalue problem (Appendix A). With $\rho_e = \boldsymbol{\nabla} \cdot \mathbf{D}$, $j_z + \partial_t D_z$ can be calculated at $z = 0$. Keeping only the horizontally homogeneous terms because of the surface integral in (1), one obtains to lowest order in A:

$$\mathcal{N}_r \simeq \frac{A^2}{2}\Big[\sigma'_a N_z(N_z - \Phi_c) + \epsilon'_\parallel \Phi_c V_z - \epsilon'_a N_z(V_z + \omega\tau_0 \Phi_s)\Big], \tag{7}$$

$$\mathcal{N}_i \simeq \frac{A^2}{2}\left[\epsilon'_a N_z(N_z - \Phi_c) + \frac{\Phi_s}{\omega\tau_0}\,(\sigma'_a N_z - \epsilon'_\parallel V_z)\right] \tag{8}$$

with $\sigma'_i = \sigma_i/\sigma_\perp$ and $\epsilon'_i = \epsilon_i/\epsilon_\perp$ for $i = a$ or $\parallel$. For standard nematic materials with large positive σ'_a (see *e.g.* (10)), the leading term in $\mathcal{N}_r$ (7) is the anisotropic conduction term in $\sigma'_a N_z^2$, which imposes a positive value of $\mathcal{N}_r$. One thus expects that the tilt of the director out of the plane in roll structures will enhance the electrical conduction of the layer and finally the in-phase current. Concerning $\mathcal{N}_i$ (8) it should be noted that Φ_s/ω tends to a finite positive value when $\omega \to 0$ (see Eq. (A.1)). Two terms of (8) control the sign of $\mathcal{N}_i$. The first term in $\epsilon'_a N_z^2$ reveals a diminution of the effective capacitance of the cell due to the director tilt, since the dielectric anisotropy ϵ'_a of the nematic materials used in electroconvection is usually negative. The other important contribution is the positive term in $\sigma'_a N_z \Phi_s/\omega$, which expresses that the potential modulation induced by the convection creates by coupling with the director tilt an out-of-phase current $I_i > 0$ (see Eq. (3)). Since Φ_s/ω decreases with ω, this positive term can compensate the negative term in $\epsilon'_a N_z^2$ at low frequencies only, and for nematics with large σ'_a.

In order to *numerically* compute precise values of $\mathcal{N}_r$ and $\mathcal{N}_i$, we use an improved version of the Fourier-Galerkin code developed in [16] to calculate weakly nonlinear roll solutions fulfilling the realistic boundary conditions

$$\mathbf{n} = \hat{\mathbf{x}}\ , \quad \mathbf{v} = \mathbf{0}, \quad \phi = 0 \quad \text{at} \ \ z = \pm d/2.$$

Fourier series are still used in the x and y directions, whereas combinations of Tchebyshev polynomials are now used to expand the z-dependence of all fields to accelerate the convergence (typically 6 z-modes were sufficient). A procedure has been written to calculate the Nusselt numbers. The current (1) is evaluated at the lower plate $z = -d/2$ where, because of the boundary conditions, $j_z + \partial_t D_z$ reduces to $(\sigma_\perp + \epsilon_\perp \partial_t) E_z$. Thus

$$I = I^0 - \sqrt{2} V \iint_S (\sigma_\perp + \epsilon_\perp \partial_t)\partial_z \phi \ \mathrm{d}x \ \mathrm{d}y \tag{9}$$

where the spatial average selects the contribution of the potential ϕ of the homogeneous quadratic slave mode noted $A^2 V_2(\mathbf{q}, -\mathbf{q})$ in equation (27) of [16]. We will return to the numerical results [18] (Fig. 3), which confirm the trends found from the analytic formulae equations (7, 8), after presenting our experimental results.

3 Experimental methods

We use an arrangement based on a pre-fabricated liquid crystal cell [19] which has *etched electrodes*, so that within the active area there is nothing besides the liquid crystal itself. Cells constructed without such electrode etching contain spacers (to maintain the separation d) and often adhesive within the current's path. These components necessarily induce unpredictable and poorly controlled contributions to the measured electric current. For example, we estimate the use of Mylar spacers without etched electrodes can alter I_i by as much as 30% [20]. Moreover, the presence of spacers and/or adhesive in the current path must result in a distortion of the nematic director in the vicinity of these objects. This distortion will not only cause the (real) measured quiescent current to deviate from $V/R_\perp$, but will also lead to rounding of the transition. So, although one may always measure the current no matter what the sample cell construction, extracting the Nusselt numbers, and observing a sharp transition in this quantity, is simply not possible without the use of etched electrodes such as in the present experiment.

In our cells, the electrodes are separated by $d = 22.3 \pm 0.5$ μm. Before the cell is filled, we measure, using an auto-balancing 1 kHz bridge, the capacitance of the cell in order to determine accurately (within 8 ppm) the ratio S/d (nominally $S = 10\,\mathrm{mm} \times 10\,\mathrm{mm}$). After this measurement the nematic liquid crystal methoxybenzylidene butyl-aniline (MBBA) [21], used as received, is introduced between the transparent conducting electrodes. The filled cell is placed in a temperature controlled housing, and then introduced between the pole faces of a large electromagnet. As the nematic liquid crystal undergoes the magnetically induced splay Frederiks transition, the capacitance and conductance of the cell are monitored. From these measurements we obtain both electric conductivities and both dielectric constants [22]. For the experiments reported here, all at 25 °C, we find

$$\begin{aligned} &\sigma_\perp = (1.5 \pm 0.01)\ 10^{-7} (\Omega\mathrm{m})^{-1}, \\ &\sigma'_a = \sigma_a/\sigma_\perp = 0.538 \pm 0.002, \\ &\epsilon_\perp = (4.81 \pm 0.01)\epsilon_0, \\ &\epsilon'_a = \epsilon_a/\epsilon_\perp = -0.1180 \pm 0.0005, \end{aligned} \tag{10}$$

with ϵ_0 the vacuum dielectric permittivity, which gives $\tau_0 = \epsilon_\perp/\sigma_\perp = (2.84 \pm 0.03)\ 10^{-4}$ s. After these measurements, the nematic cell is transferred to the stage of a polarizing microscope so that shadowgraph [7] images can be obtained concomitantly with the electric current measurements. A function generator is used to produce a sinusoidal voltage signal which is in turn amplified, and applied to the cell. The path-to-ground for the current traversing the cell is through a current-to-voltage converter. The output signal from this converter is measured by a lock-in amplifier, whose reference signal is supplied by the original function generator. Before any measurements are taken, the nematic cell is replaced by a purely resistive load and the phase setting on the lock-in is adjusted to zero the out-of-phase current component. The nematic

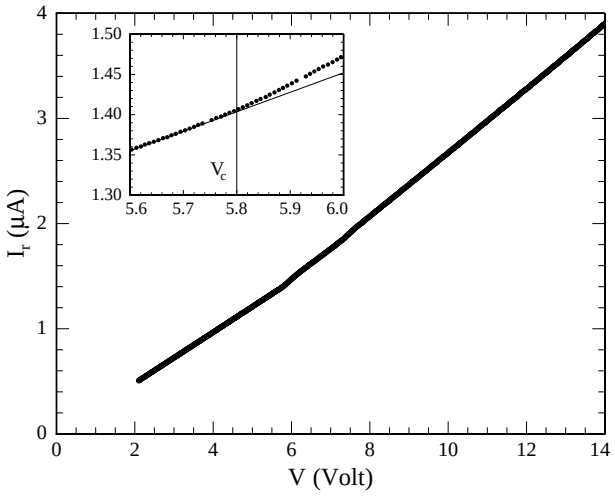

Fig. 1. In-phase current I_r *vs.* the applied voltage V at a frequency $\omega/(2\pi) = 100$ Hz *i.e.* $\omega\tau_0 = 0.18$. *Inset:* blowup of the neighbourhood of V_c.

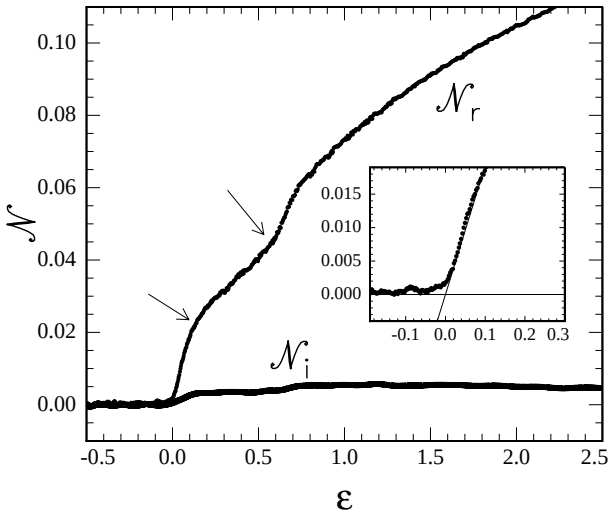

Fig. 2. Real and imaginary reduced Nusselt numbers *vs.* the distance to threshold ϵ for electroconvection of MBBA at the same frequency as in Figure 1. The arrows indicate knees apparently linked with secondary instabilities (see text). Inset: blowup of the small ϵ region indicating how $\mathcal{N}_r$ initially increases linearly with ϵ.

cell is then re-inserted. Then, at a selected frequency V is raised in small steps. At each step, after waiting several seconds, I_r and I_i are recorded [23]. This proceeds until a maximum desired V (well above the threshold value V_c) is reached. Then, the process is reversed, and the currents recorded as V decreased. The difference in current for increasing *vs.* decreasing V is less than 2%. When V is raised above V_c, the electric current traversing the liquid crystal measurably deviates from its value in the quiescent state, I^0. In order to determine V_c from either the in-phase or out-of-phase current data, we first determine a baseline for I_r^0 (I_i^0) by fitting a straight line to I_r (I_i) *vs.* V for V much smaller than V_c; see Figure 1. These values of I_r^0/V and I_i^0/V provide independent measurement of $\sigma_\perp$ and $\epsilon_\perp$ (see Eq. (2)) that agree within 5% with the direct measurement of these parameters using the Frederiks transition. The Nusselt numbers as functions of V are then calculated by subtracting unity from the ratios I_r/I_r^0 and I_i/I_i^0 . By fitting another straight line to $\mathcal{N}_r$ ($\mathcal{N}_i$) in the region where it deviates from zero, we define V_c as where this line crosses zero (see the insets in Figs. 1 and 2). Using this technique, the imprecision in determining V_c is about 0.2%. In the inset of Figure 2, pretransitional effects are visible. These effects are small: $\mathcal{N}_r$ remains below 0.0015 below V_c as determined using the process described above; our accuracy in measuring $\mathcal{N}_r$ is about 0.0004. Since the electric current represents an average over the entire conducting area, pretransitional effects are expected from any and all inhomogeneities within the conducting area, including imperfections in surface alignment, dust particles and fringing fields at the edge of the conducting area. Concomitant shadowgraph observations obtained by examining several regions within the conducting area reveal that electroconvective rolls arise at a potential difference within 0.2% of V_c as determined by the process described above.

Our apparatus did not reach sufficiently large V to measure the crossover to the dielectric regime (see *e.g.* [3,15]); we therefore estimated a characteristic "cut-off" frequency ω_c by fitting $V_c(\omega)$ to equation (A.3). We found typically $\omega_c/(2\pi) = 1400 \pm 21$ Hz, but during the course of taking the measurements (2-3 months) this quantity varied by $\pm 5\%$, probably in connection with variations of the electrical parameters, especially the conductivities.

4 Experimental results - Comparison with the theory

In Figure 2 we plot both the real and imaginary Nusselt numbers *vs.* ϵ. For the data sets shown here, both Nusselt numbers are positive. In general, $\mathcal{N}_r$ is always observed to be positive; as discussed subsequently, $\mathcal{N}_i$ can be either positive or negative above the onset of convection. Note also that $\mathcal{N}_r$ is at least ten times larger in magnitude than $\mathcal{N}_i$.

In the region below threshold, where the threshold is found in the way specified above, the magnitude of $\mathcal{N}_r$ averages less than 0.0005, and it never exceeds 0.0015. The lowest value of $\mathcal{N}_r$ that we can reliably measure is roughly 0.0004. Thus, below threshold, $\mathcal{N}_r$ is as close to zero as we can detect. At $\epsilon = 0$, this quantity abruptly grows from zero. Thus, we have a sharp, supercritical bifurcation. Close to threshold, *i.e.* for $0 \leq \epsilon \lesssim 0.1$, both Nusselt numbers are proportional to ϵ as shown in the inset for the real Nusselt number: this confirms the supercritical law $A \sim \sqrt{\epsilon}$. The variations of the corresponding slopes $\mathcal{N}_r/\epsilon$ and $\mathcal{N}_i/\epsilon$ *vs.* $\omega\tau_0$ are given in Figure 3, which represents the results of several ramps in ϵ at each frequency.

To compare these results with the theoretical predictions of the SM, we use, in the Fourier-Galerkin code, the elastic constants and the viscosities measured for MBBA

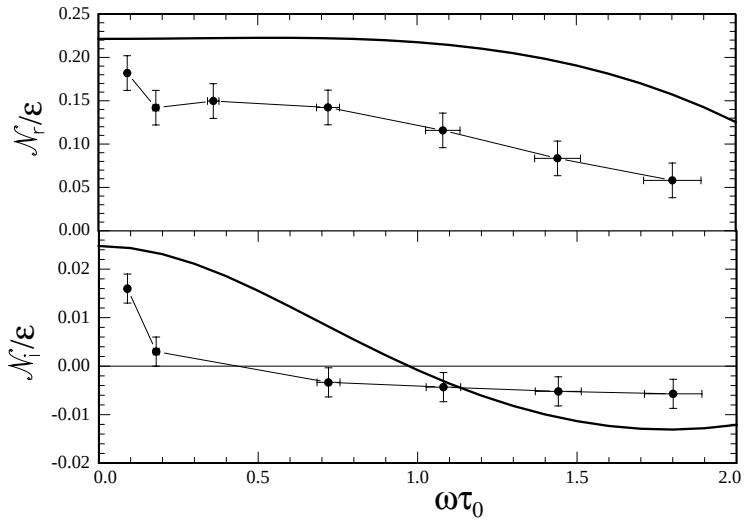

Fig. 3. Black circles: measured ratios $\mathcal{N}_r/\epsilon$ and $\mathcal{N}_i/\epsilon$ at small ϵ *vs.* the dimensionless frequency. Note that the measurements span a decade in frequency. The vertical error bars correspond to the imprecision in measuring $\mathcal{N}/\epsilon$ and to the dispersion between different ϵ ramps, while the horizontal error bars originate from the variation in the charge-diffusion time τ_0. Solid lines: prediction from weakly nonlinear SM calculations.

at 25 °C in [24,25], and the electric parameters that we determined independently (*cf.* equation (10)). We calculate, with a fit to equation (A.3), for the "cutoff" frequency $\omega_c/(2\pi) = 1260 \pm 20$ Hz, in rough agreement with the measured value. We also calculate, with the weakly nonlinear numerical code introduced Section 2.2, the values of $\mathcal{N}_r/\epsilon$ and $\mathcal{N}_i/\epsilon$ (Fig. 3). The measurements of both the real and imaginary Nusselt numbers agree with our calculations within about a factor of two; agreement for $\mathcal{N}_i$ is better. Moreover, both quantities exhibit the dependence on $\omega\tau_0$ we predict, although $\mathcal{N}_i/\epsilon$ crosses zero at a smaller value of $\omega\tau_0$ than predicted. The partial agreement with theory shown here is significant in light of the fact that, contrarily to the standard approach in nematic electroconvection where usually $\sigma_\perp$ is fitted, *no* parameters have been adjusted.

Deviations from the weakly nonlinear regime are seen in the experiments when ϵ becomes of order of 0.1, where the curves of $\mathcal{N}$ *vs.* ϵ deviate from straight lines (Fig. 2). The corresponding "knees" apparently indicate the onset of secondary instabilities. For instance, in the region pointed by the first arrow in Figure 2, the patterns observed optically show a continuous transition from normal rolls to undulated rolls; this corresponds to the undulation zig-zag instability [26]. The transition seen in the patterns and the knee on the $\mathcal{N}$ *vs.* ϵ curves are both not sharp, which makes a quantitative identification of the two secondary "thresholds" tedious. We note also that a theoretical estimation of the undulation zigzag threshold [16] for our material parameters gives at $\omega\tau_0 = 0.18$, $\epsilon_{ZZ} = 0.06 \pm 0.01$. This appears to be smaller than the value deduced from the first knee of Figure 2, $\epsilon_{ZZ} \simeq 0.10$. However this type of discrepancy between experimental zigzag thresholds and the SM is well known for MBBA, see *e.g.* the typical values for ϵ_{ZZ} found recently in [27]. On the other hand, optical observations of the convective patterns shows that the knee pointed by the second arrow in Figure 2 is probably connected to spontaneous generation of dislocations associated with the so-called "defect chaos" [14]. In [9], similar effects were seen: a dramatic increase in effective conductance at the onset of convection, as well as secondary instabilities.

5 Conclusion

One obvious reason to explain the remaining discrepancies between our measurements and the SM predictions is that we have used tabulated values of the elastic constants and the anisotropic viscosities for these calculations, and that these material parameters might be different for our actual MBBA. However it is highly unlikely that these factors alone could lead to the factor of two discrepancy shown in Figure 3. Therefore we believe that the discrepancies that we evidence reveal a shortcoming of the SM. In fact, nematic liquid crystals are clearly electrolytic conductors, *i.e.* the Ohmic conduction assumed in the SM introduces an important approximation. The so-called weak electrolyte model (WEM) has been introduced recently as a new model in which the electrical conductivity is assumed to be due to two species of dissociated ions having different mobilities [28]. It would be interesting to develop a theoretical calculation of the electric Nusselt numbers within the WEM; one difficulty is that new material parameters are then to be introduced and measured or fitted [28]. In any cases our measurements will provide a precise, quantitative test of nematic electroconvection models, both concerning the threshold voltage as well as weakly nonlinear or strongly nonlinear properties, including secondary instabilities. Moreover the characterization method developed here, always fully quantitative, can be applied successfully to the study of the challenging

"fully anisotropic turbulent regimes" that occur at very large ϵ [13,12].

J.T.G. and N.G. acknowledge technical assistance from A.R. Baldwin. Their work was supported by Kent State University, the Ohio Board of Regents and NSF grant no. DMR-9988614. E.P. thanks B. Dressel and W. Pesch for very fruitful discussions and comparisons with their code.

Appendix A: Quasi-unidimensional model

Within the quasi-unidimensional model, the critical mode amplitudes (see Eq. (6)) read

$$\begin{aligned} \Phi_c &= \varphi(\omega)\ [\sigma'_\parallel \sigma'_a + \epsilon'_\parallel \epsilon'_a (\omega\tau_0)^2]\ N_z, \\ \Phi_s &= \varphi(\omega)\ (\sigma'_\parallel - \epsilon'_\parallel)\ \omega\tau_0\ N_z, \\ V_z &= (\epsilon_\parallel \Phi_c - \epsilon_a N_z) \frac{\tau_0 V_c^2}{\nu d^2}, \end{aligned} \tag{A.1}$$

where $\varphi(\omega) = (\sigma'_\parallel)^{-2}[1 + (\omega\tau_1)^2]^{-1}$, $\tau_1 = \epsilon_\parallel/\sigma_\parallel$, $\nu = (\alpha_4 + \alpha_5 - \alpha_2)/2$ is a characteristic viscosity, and

$$V_c = \sqrt{\frac{k_{33}\nu\pi^2}{\epsilon_\perp\{\sigma'_\parallel \sigma'_a \nu'(\omega) + \epsilon'_a[\alpha_2 + \nu + \epsilon'_\parallel \nu'(\omega)(\omega\tau_0)^2]\}}}, \tag{A.2}$$

with k_{33} the bend elastic constant, $\nu'(\omega) = -\varphi(\omega)(\epsilon'_\parallel \alpha_2 + \epsilon'_a \nu)$, is an estimate of the onset electrical potential. Note that V_c^2 assumes the form

$$V_c^2 = V_0^2 \frac{1 + (\omega\tau_1)^2}{\omega_c^2 - \omega^2}\ , \tag{A.3}$$

which has been used, with V_0, τ_1 and ω_c as free parameters, in order to determine the cutoff frequency ω_c; indeed such an ω-dependence is also expected within more precise models, see *e.g.* the equation (3.11) of [10].

References

1. H. Bénard, Ann. Chimie Phys. **23**, 62 (1901); L. Rayleigh, Phil. Mag. **32**, 529 (1916).
2. W. Helfrich, J. Chem. Phys. **51**, 4092 (1969).
3. Orsay Liquid Crystal Group, Phys. Rev. Lett. **25**, 1642 (1970).
4. R.J. Schmidt, S.W. Milverton, Proc. Roy. Soc. (Lond.) A **152**, 486 (1935).
5. J. Liu, G. Ahlers, Phys. Rev E **55**, 6950 (1997).
6. X. Chavanne *et al.*, Phys. Rev. Lett. **79**, 3648 (1997).
7. S. Rasenat, G. Hartung, B.L. Winkler, I. Rehberg, Exp. Fluids **7**, 412 (1989); A. Joets, R. Ribotta, J. Phys. I France **4**, 1013 (1994).
8. T. Kai, S. Kai, K. Hirakawa, J. Phys. Soc. Jpn **43**, 717 (1977).
9. I. Rehberg, B.L. Winkler, M. de la Torre-Juarez, S. Rasenat, W. Schöpf, Festkörperprobleme **29**, 35 (1989).
10. E. Bodenschatz, W. Zimmermann, L. Kramer, J. Phys. France **49**, 1875 (1988).
11. W.I. Goldburg, Y.Y. Goldschmidt, H. Kellay, Phys. Rev. Lett. **87**, 245502 (2001).
12. J.T. Gleeson, Phys. Rev. E **63**, 026306 (2001).
13. S. Kai, K. Hirakawa, Supp. Prog. Theor. Phys. **64**, 212 (1978).
14. S. Kai, W. Zimmermann, Prog. Theor. Phys. Sup. **99**, 458 (1989); E. Braun, S. Rasenat, V. Steinberg, Europhys. Lett. **15**, 597 (1991).
15. L. Kramer, E. Bodenschatz, W. Pesch, W. Thom, W. Zimmermann, Liq. Cryst. **5**, 699 (1989).
16. E. Plaut, W. Pesch, Phys. Rev. E **59**, 1747 (1999).
17. From calculations of the type of those presented in Section 2.2, but including higher temporal harmonics of all fields, we expect (at $\omega\tau_0 \simeq 1$) the higher temporal harmonics of the current to be of the order of 1 nA, to be compared with the 1 μA or so of I_r and I_i. These order of magnitudes are confirmed by the experiments [23].
18. Numerical predictions for $1 + \mathcal{N}_r$ have also been given in Figure 16c of [10]. Using the same material parameters "MBBA 2", our code gives the nonlinear quantities plotted in Figure 16a, b of [10], but different values for the real Nusselt number (*e.g.* $\mathcal{N}_r = 0.19$ at $\omega = 0$ instead of 0.38 in [10]). Since no explanations were provided in [10] concerning the method of calculation of the Nusselt number, we cannot explain the origin of this discrepancy, but we note that our values are more consistent with the one measured for MBBA.
19. E.H.C. Co, Tokyo, Japan.
20. In the quiescent state below threshold, one then expects

$$I_i^0 = \frac{\sqrt{2} V \omega}{d} (\epsilon_{lc} S_{lc} + \epsilon_{\rm spacer} S_{\rm spacer}).$$

The order of magnitude of the corrections induced by a Mylar spacer is (for the relative dielectric constant of Mylar, see `www.goodfellow.com`)

$$r \ = \ \frac{\epsilon_{\rm spacer}}{\epsilon_{lc}} \ \frac{S_{\rm spacer}}{S_{lc}} \ \simeq \ \frac{3}{5} \ \frac{1\ {\rm cm}^2}{2\ {\rm cm}^2} \ \simeq \ 0.3$$

which is not small. These corrections will introduce a larger error on the electric Nusselt number $\mathcal{N}_i$ in the convection regime.

21. Frinton Laboratories, Vineland, NJ.
22. At zero magnetic field H, the cell's resistance is $R_\perp = d/(\sigma_\perp S)$ and the capacitance $C_\perp = \epsilon_\perp S/d$; as H becomes larger than the Frederiks threshold value, we fit the $R(H), C(H)$ data to obtain the values of σ'_a, ϵ'_a.
23. After this delay I_r and I_i always reach a stationary value. We also use the digital signal processing capability of the lock-in amplifier to measure higher temporal harmonics of the current; these are found to always be at least two orders of magnitude smaller than the fundamental.
24. W.H. de Jeu, W.A.P. Claassen, A.M. Spruijt, Mol. Cryst. Liq. Cryst. **37**, 269 (1976).
25. H. Kneppe, F. Schneider, N.K. Sharma, J. Chem. Phys. **77**, 3203 (1982).
26. R. Ribotta, A. Joets, Lin Lei, Phys. Rev. Lett. **56**, 1595 (1986) or E. Plaut, L. Pastur, R. Ribotta, Eur. Phys. J. B **5**, 283 (1998).
27. S. Rudroff, H. Zhao, L. Kramer, I. Rehberg, Phys. Rev. Lett. **81**, 4144 (1998).
28. M. Dennin, M. Treiber, L. Kramer, G. Ahlers, D. Cannell, Phys. Rev. Lett. **76**, 319 (1996).